Methods to assess sensitivity of optical coherence tomography systems

ANANT AGRAWAL,[1,*] **T. JOSHUA PFEFER,**[1] **PETER D. WOOLLIAMS,**[2] **PETER H. TOMLINS,**[3] **AND GEORGE NEHMETALLAH**[4]

[1]*Center for Devices and Radiological Health, Food and Drug Administration, Silver Spring, MD, USA*
[2]*Functional Materials Group, National Physical Laboratory, Teddington, UK*
[3]*Barts and The London School of Medicine and Dentistry, Queen Mary University of London, E1 1BB, London, UK*
[4]*Department of Electrical Engineering and Computer Science, The Catholic University of America, Washington, DC, USA*
[*]*anant.agrawal@fda.hhs.gov*

Abstract: Measuring the sensitivity of an optical coherence tomography (OCT) system determines the minimum sample reflectivity it can detect and provides a figure of merit for system optimization and comparison. The published literature lacks a detailed description of OCT sensitivity measurement procedures. Here we describe a commonly-used measurement method and introduce two new phantom-based methods, which also offer a means to directly visualize low reflectivity conditions relevant to biological tissue. We provide quantitative results for the three methods from different OCT system configurations and discuss the methods' advantages and disadvantages.

References and links

1. A. Agrawal, M. A. Gavrielides, S. Weininger, K. Chakrabarti, and T. J. Pfefer, "Regulatory perspectives and research activities at the FDA on the use of phantoms with in vivo diagnostic devices," Proc. SPIE **6870**, 687005 (2008).
2. M. Brezinski, *Optical Coherence Tomography: Principles and Applications* (Elsevier, 2006).
3. R. Leitgeb, C. Hitzenberger, and A. Fercher, "Performance of Fourier domain vs. time domain optical coherence tomography," Opt. Express **11**(8), 889–894 (2003).
4. E. A. Swanson, D. Huang, M. R. Hee, J. G. Fujimoto, C. P. Lin, and C. A. Puliafito, "High-speed optical coherence domain reflectometry," Opt. Lett. **17**(2), 151–153 (1992).
5. M. Choma, M. Sarunic, C. Yang, and J. Izatt, "Sensitivity advantage of swept source and Fourier domain optical coherence tomography," Opt. Express **11**(18), 2183–2189 (2003).
6. Z. Yaqoob, J. Wu, and C. Yang, "Spectral domain optical coherence tomography: a better OCT imaging strategy," Biotechniques **39**(6 Suppl), S6–S13 (2005).
7. R. C. Haskell, D. Liao, A. E. Pivonka, T. L. Bell, B. R. Haberle, B. M. Hoeling, and D. C. Petersen, "Role of beat noise in limiting the sensitivity of optical coherence tomography," J. Opt. Soc. Am. A **23**(11), 2747–2755 (2006).
8. J. M. Schmitt, A. R. Knüttel, A. H. Gandjbakhche, and R. F. Bonner, "Optical characterization of dense tissues using low-coherence interferometry," Proc. SPIE **1889**, 197–211 (1993).
9. B. D. Goldberg, B. J. Vakoc, W. Y. Oh, M. J. Suter, S. Waxman, M. I. Freilich, B. E. Bouma, and G. J. Tearney, "Performance of reduced bit-depth acquisition for optical frequency domain imaging," Opt. Express **17**(19), 16957–16968 (2009).
10. S. Yun, G. Tearney, B. Bouma, B. Park, and J. de Boer, "High-speed spectral-domain optical coherence tomography at 1.3 µm wavelength," Opt. Express **11**(26), 3598–3604 (2003).
11. N. Nassif, B. Cense, B. Park, M. Pierce, S. Yun, B. Bouma, G. Tearney, T. Chen, and J. de Boer, "In vivo high-resolution video-rate spectral-domain optical coherence tomography of the human retina and optic nerve," Opt. Express **12**(3), 367–376 (2004).
12. M. A. Choma, K. Hsu, and J. A. Izatt, "Swept source optical coherence tomography using an all-fiber 1300-nm ring laser source," J. Biomed. Opt. **10**(4), 044009 (2005).
13. H. Lim, J. F. de Boer, B. H. Park, E. C. W. Lee, R. Yelin, and S. H. Yun, "Optical frequency domain imaging with a rapidly swept laser in the 815-870 nm range," Opt. Express **14**(13), 5937–5944 (2006).

14. V. D. Nguyen, N. Weiss, W. Beeker, M. Hoekman, A. Leinse, R. G. Heideman, T. G. van Leeuwen, and J. Kalkman, "Integrated-optics-based swept-source optical coherence tomography," Opt. Lett. **37**(23), 4820–4822 (2012).
15. R. A. Leitgeb, M. Villiger, A. H. Bachmann, L. Steinmann, and T. Lasser, "Extended focus depth for Fourier domain optical coherence microscopy," Opt. Lett. **31**(16), 2450–2452 (2006).
16. D. Lorenser, C. Christian Singe, A. Curatolo, and D. D. Sampson, "Energy-efficient low-Fresnel-number Bessel beams and their application in optical coherence tomography," Opt. Lett. **39**(3), 548–551 (2014).
17. P. D. Woolliams, National Physical Laboratory, Hampton Road, Teddington, Middlesex, TW11 0LW United Kingdom (internal report, 2009).
18. D. X. Hammer, R. D. Ferguson, M. Mujat, A. Patel, E. Plumb, N. Iftimia, T. Y. P. Chui, J. D. Akula, and A. B. Fulton, "Multimodal adaptive optics retinal imager: design and performance," J. Opt. Soc. Am. A **29**(12), 2598–2607 (2012).
19. D. X. Hammer, A. Lozzi, E. Abliz, N. Greenbaum, A. Agrawal, V. Krauthamer, and C. G. Welle, "Longitudinal vascular dynamics following cranial window and electrode implantation measured with speckle variance optical coherence angiography," Biomed. Opt. Express **5**(8), 2823–2836 (2014).
20. M. N. Polyanskiy, "Refractive index database," http://refractiveindex.info
21. P. H. Tomlins, G. N. Smith, P. D. Woolliams, J. Rasakanthan, and K. Sugden, "Femtosecond laser micro-inscription of optical coherence tomography resolution test artifacts," Biomed. Opt. Express **2**(5), 1319–1327 (2011).
22. A. Agrawal, S. Huang, A. Wei Haw Lin, M. H. Lee, J. K. Barton, R. A. Drezek, and T. J. Pfefer, "Quantitative evaluation of optical coherence tomography signal enhancement with gold nanoshells," J. Biomed. Opt. **11**(4), 041121 (2006).
23. S. Prahl, "Mie scattering," http://omlc.org/software/mie.
24. C. Maetzler, Institute of Applied Physics, University of Bern, Sidlerstrasse 5, 3012 Bern, Switzerland (internal report, 2002).
25. C. E. Papadopoulous and H. Yeung, "Uncertainty estimation and Monte Carlo simulation method," Flow Meas. Instrum. **12**(4), 291–298 (2001).

1. Introduction

Optical coherence tomography (OCT) has been established as an incredibly sensitive method to image tiny, weakly reflecting objects, such as micron-scale biological structures, even when buried beneath relatively thick light-attenuating material. With nearly every new OCT configuration described in the literature over the past 25 years, the system signal-to-noise ratio (SNR) has also been reported to extol that OCT system's virtue with respect to sensitivity. Measuring the sensitivity of an OCT system is an important characterization step, as it establishes the minimum reflectivity the system can detect, and it offers a means for comparing or tracking system performance with direct relevance to image quality. The tradeoff between image quality and critical system parameters like illumination power and image acquisition speed is revealed via the sensitivity. The importance of sensitivity as a figure of merit in medical imaging has been formally recognized: a federal regulation requires the sensitivity of all x-ray mammography devices in US clinics to be assessed weekly with a phantom [1]. Though we often see the sensitivity values of OCT reported, little documentation exists in the literature about measurement procedures and calculations for determining SNR.

1.1 Definition of OCT sensitivity

Sensitivity is the minimum sample reflectivity required to achieve SNR = 1 [2,3]. Since the early days of OCT, SNR has been calculated as [3–7]

$$SNR = \left(\frac{I_{samp}}{\sigma_{bg}}\right)^2,$$

(1a)

which in decibels (dB) corresponds to

$$SNR\,(\mathrm{dB}) = 20\log\left(\frac{I_{samp}}{\sigma_{bg}}\right).$$

(1b)

I_{samp} is the background-subtracted image intensity from a reflecting object placed in the interferometer's sample arm, and σ_{bg} is the standard deviation of the image background intensity (i.e., with no sample present). Squaring the signal and noise terms is needed to convert OCT image intensity values, proportional to the amplitude of the interference fringes resulting from cross-correlation of sample and reference fields, to power values. From established formulas for the OCT image intensity [5,6,8], SNR is expected to be proportional to the sample reflectance R, shown in Eq. (2a) with proportionality constant K, which lumps light source intensity and system noise properties. Since R can have a value only between 0 and 1, SNR is maximized (SNR_{max}) when $R = 1$ [Eq. (2b)]. In addition, we introduce R_{min} as the reflectance to achieve SNR = 1, which is the sensitivity criterion [Eq. (2c)]:

$$SNR = K \cdot R, \tag{2a}$$

$$SNR_{max} = K \cdot 1, \tag{2b}$$

$$1 = K \cdot R_{min}. \tag{2c}$$

Substituting the value of K from Eq. (2b) into Eq. (2c) we obtain a simple relationship between R_{min} and SNR_{max}:

$$R_{min} = \frac{1}{SNR_{max}}. \tag{3}$$

R_{min} or SNR_{max} can be used to express sensitivity for an OCT system with linear response to sample reflectance.

1.2 Previous measurement work

At the time when Fourier domain OCT was first appearing, Leitgeb et al. briefly described a technique to measure its sensitivity for comparison to time domain OCT, by recording the image intensity at different reflectivity levels with a neutral density filter in the sample arm [3]. With a similar goal in mind, Choma et al. examined the sensitivity advantage of spectral domain and swept source OCT configurations over time domain [5]. Their measurement procedure, not explicitly described, apparently follows a similar approach to Leitgeb et al. through the use of "calibrated sample arm attenuation." Goldberg et al. also used this type of sensitivity measurement as a figure of merit to compare different digitization bit depths in acquired swept source OCT signals [9]. Since Fourier domain OCT inherently exhibits a reduction in sensitivity with increasing axial distance, numerous OCT system developers have characterized this so-called "signal rolloff" for their spectrometer-based [10,11] and swept source [12–14] OCT realizations by axial translation of a specular reflector. Instead of using a specular surface, several works have employed microparticle phantoms for SNR/sensitivity analysis [14–16], though absolute sensitivity measurement was not reported.

The National Physical Laboratory wrote an internal report with great detail on sensitivity measurement, including an illustration of the measurement setup, different attenuation and reflector options, data analysis methods and uncertainty estimation [17]. This measurement procedure is summarized and applied here. Since a perfectly reflecting sample would saturate the photodetector, an attenuated reflector is used and the measured SNR is adjusted by the attenuation value to obtain SNR_{max}. The typical measurement setup resembles that shown in Fig. 1, wherein a reflector is placed normal to the OCT beam at its focal position with an attenuating filter between the OCT front optic and the reflector [17]. The reflector has an optically flat surface and provides a known reflectivity, such as a polished fused silica glass plate. Its position normal to the beam with its front surface coincident with the beam focus ensures all the reflected light is captured from the front surface.
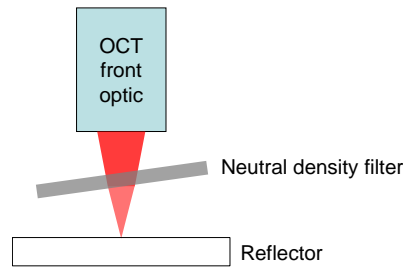
Fig. 1. Conventional OCT sensitivity measurement setup.

In the case of a transparent reflector like fused silica, its thickness should be at least several millimeters or its back surface wedged to cause any back surface reflection to be substantially weaker than and/or separate from the front surface reflection in the OCT image. The filter's attenuation must also be well-known and tilt-invariant, so a spectrally calibrated metal-on-glass neutral density filter serves this purpose well. The filter should be tilted slightly so the OCT system does not capture its reflection, which could corrupt the signal from the reflector. To obtain the correct SNR_{max} value which has accounted for the filter and reflector (i.e., as if measuring SNR with a perfect reflector), a modified form of Eq. (1b) is used [17]:

$$SNR_{max}(\text{dB}) = 20\log\left(\frac{I_{samp}}{\sigma_{bg}}\right) - 10\log\left(R_{samp}T_{filt}{}^2\right), \qquad (4)$$

where R_{samp} is the reflectance of the specular reflector as the sample, and T_{filt} is the transmittance of the attenuating filter (including specular losses). Transmittance is squared to account for the double pass through the filter. The multiplicative factor of 10 instead of 20 is applied to the reflectance/transmittance term since R and T are power values.

The technique described above provides for quantification of sensitivity via careful SNR measurement under strong signal conditions. It requires precise positioning of the reflector and filter, accurate knowledge of their respective reflectance and transmittance, and the OCT front optic must offer sufficient working distance to accommodate the tilted filter and its holder. However, for periodic checks on system performance, particularly in a clinical setting with OCT users having less technical training, a simpler, quicker, and/or automated method to assess sensitivity (or at least changes in it) would be quite beneficial. The x-ray mammography phantom mentioned above contains a known pattern of objects of varying size and x-ray density and requires the user to simply identify which objects can be detected visually. In addition, a more direct and relevant way to quantify OCT sensitivity is to perform the measurement under conditions which replicate tissue optics near R_{min}, to yield SNR close to 1 (0 dB).

1.3 Overview of study

This study presents and compares several methods to assess OCT sensitivity: (1) a conventional method of measuring SNR_{max} with a specular surface, (2) using a commercially-available laser-inscribed phantom, and (3) using a collection of phantoms made from suspensions of weakly-scattering silica microspheres. The last two methods are specifically conceived and implemented to improve the convenience and information content of sensitivity measurements. Quantitative SNR calculations for each of the assessment methods with different OCT device configurations then provide information on the relative strengths and weaknesses of each method to characterize sensitivity. Although OCT images are typically scaled and displayed in logarithmic intensity units to enhance visualization of weaker signals, these display-related transformations shall not be considered in the sensitivity

measurements and calculations here; instead, the raw linear intensity values output after standard OCT signal processing shall be used in the interest of objectivity and for ease in comparing results quantitatively.

2. Materials and methods

2.1 OCT instrumentation

To understand sensitivity measurement issues under different OCT operating conditions, this study was performed with two laboratory spectral domain OCT (SDOCT) systems−one operating at 855 nm nominal source wavelength [18] and the other at 1310 nm [19]. These two source wavelengths are the most common in clinical devices, the former mainly used for ophthalmic imaging. Both systems comprise a superluminescent diode illumination source, fiber optic interferometer, and spectrometer with transmission grating and line-scan camera. The 855 nm system includes adaptive optics enhancement capability which was disabled for this study. Table 1 lists the major parameters of the systems which strongly influence sensitivity. The power at the sample is perhaps the most influential on this list, so multiple power levels for the 1310 nm system were investigated. The 855 nm system had no provision for power adjustment, and adjustment of the other parameters was not possible without affecting other performance factors. For example, adjusting camera integration time must be coupled with an adjustment of the galvanometer scan speed or amplitude, which alters the magnitude of SNR-degrading mechanical vibrations in the scanners. The spot size and numerical aperture (NA) come into play in sensitivity determination as the sample properties are varied. The number of pixels in an A-scan and B-scan are important to keep in mind when deciding how many pixels to include in statistical calculations. B-scan width was chosen to be near the hardware limit, for broad spatial sampling. All statistical measures of OCT intensity (mean and standard deviation) used in this study were taken offline, after recording individual B-scans.

Table 1. OCT system parameters

	855	1310
Center wavelength (nm)	**855**	**1310**
FWHM* spectral bandwidth (nm)	56	84
FWHM coherence length (μm)	6	9
Power at sample (mW)	0.6	1.2, 2.3, 4.5
Illumination spot diameter at focus (μm)	12	9
Collection NA	0.04	0.12
Camera integration time (μs)	49	13
A-scan length (pixels)	1024	1024
A-scans per B-scan	1024	500
B-scan width (mm)	1.5	1.5

*FWHM: full-width at half-maximum

2.2 Specular surface

Conventional SNR measurements using the setup shown in Fig. 1 require a specular reflector as the phantom, along with an attenuating filter chosen to reduce the reflector's signal below the system saturation level. For this study, the attenuating filter was from a calibrated set of metal-on-glass neutral density filters (TFS-ND06-02c, Avian Technologies, Sunapee, NH), whose transmittance values measured by the manufacturer are traceable to National Institute of Standards and Technology (NIST) values. For the 855 nm system, a filter with nominal optical density (OD) of 1 was used, whereas an OD = 2 filter was used for the 1310 nm system since its output power was considerably higher. The filter was mounted in a fixed holder with its surface tilted just enough to prevent specular reflections from entering the OCT front optic.

The reflector for these measurements was a laser-grade fused silica block (SQW-0525-UV, CVI Laser Optics, Albuquerque, NM) with exceptionally high specular surface quality (10-5 scratch and dig) and a thickness of 6 mm. Its reflectance in air was calculated using the well-known Fresnel equation for the case when light is normally incident on a specular surface: $R_{samp} = (n_1-n_2)^2/(n_1 + n_2)^2$, where n_1 is the refractive index of fused silica (1.453 at 855 nm, 1.447 at 1310 nm [20]) and assuming $n_2 = 1$ for air. The fused silica block was placed on a mount which enabled fine vertical translation and two-axis tilt adjustment to maximize signal return, which implies all of the reflected light is captured by the OCT front optic. Table 2 provides the values of R_{samp} and T_{filt} needed to calculate SNR_{max} with Eq. (4). For T_{filt}, the mean transmittance of the filter across each OCT system's FWHM spectral bandwidth was taken; for reference, the transmittance standard deviation is also shown in Table 2.

Table 2. Reflectance and transmittance values for SNR_{max} calculations

OCT source wavelength (nm)	R_{samp}	T_{filt}
855	0.034	0.12 ± 0.0003
1310	0.033	0.045 ± 0.0008

2.3 Laser-inscribed phantom

2.3.1 Phantom overview

A phantom specifically designed for OCT imaging performance testing has recently become commercially available (ALS-OP01, Arden Photonics, West Midlands, UK). It contains four separate regions, each containing a unique pattern of subsurface thin lines to enable measurement of a specific parameter: point spread function (PSF), sensitivity, lateral resolution, and distortion. The phantom is a fused silica plate in which the patterns have been inscribed with a femtosecond-pulsed laser. Non-linear absorption at the focal spot of the laser modifies the local refractive index; scanning the focal spot through the silica forms embedded lines which diffusely scatter light. The sensitivity pattern consists of six groups of lines placed side-by-side, with line width increasing from Group 1 to Group 6 and within each group as well. This format is similar to the mammography phantom, which is designed to enable imaging personnel report which objects are visible in the image. Line width is dependent on the laser inscription energy (higher energy yields a wider line), and in turn reflectivity is directly related to line width [21]. As illustrated in Fig. 2, the lines in a group are separated by "index" lines for ease of use: Group x has x index lines on the left and $x + 1$ index lines on the right. Lines are inscribed at different depths and are staggered laterally to prevent blocking of reflections from deeper lines by shallower lines.
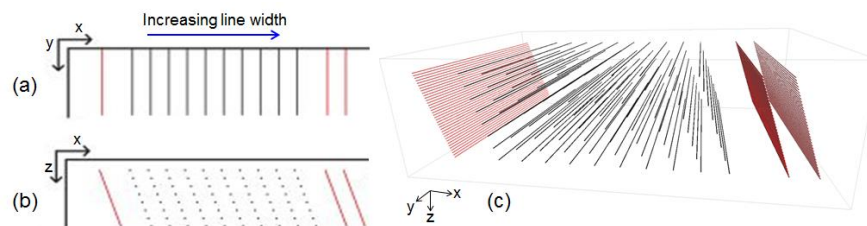

Fig. 2. Schematic of single group in sensitivity region of laser-inscribed phantom. (a) Top/*en face* view. (b) Side/B-scan view. (c) 3D perspective view. Group lines are in black, index lines are in red. Though not apparent in this schematic, group line width increases from left to right.
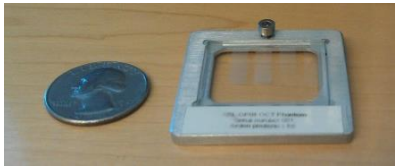
Fig. 3. Photograph of laser-inscribed phantom.

2.3.2 Phantom characterization

Figure 4 shows light microscopy images of individual sensitivity lines in the top row of the phantom. The microscope was configured with oblique illumination, a 20X/0.5 NA objective, and charge-coupled device (CCD) camera. The bright appearance of the lines under oblique illumination indicates they scatter light over a broad angular extent, though the scattering is quite variable along each line. The apparent similarity in brightness of the lines in Fig. 4 results from autoscaling each image; Fig. 5 shows the actual brightness of these lines, along with their measured FWHM. Line width and brightness increase significantly from the first to last line within each group, and the first line of Group $x + 1$ has similar width and brightness as the last line of Group x. The width of Group 1/Line 1 approaches the resolution limit of the microscope, and even Group 6/Line 10, the thickest of all the lines, is well below the resolution of typical OCT systems. Deeper lines have similar widths (data not shown). Group 1 contains only 6 lines in its top row, unlike the other groups having 10 lines. This discrepancy occurs since the laser inscription process is a threshold phenomenon, dependent on the material and laser properties [21], so thinner and less reflective lines could not be realized. The relative variability in width was greatest for Group 1/Line 1 (18% coefficient of variation), suggesting inscription was occurring very close to the threshold conditions.
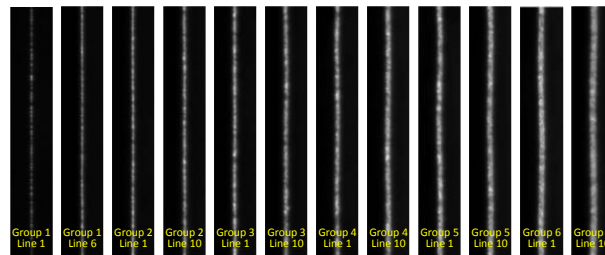

Fig. 4. Oblique illumination microscopy images of individual lines in the sensitivity region of laser-inscribed phantom. Images are 22 μm wide × 134 μm high. Brightness of each image is autoscaled to show detail.
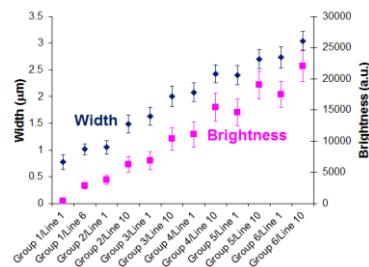

Fig. 5. Measured width and brightness of lines shown in Fig. 4. Error bars represent the standard deviation of the measurement across each image.

2.4 Microsphere suspension phantoms

Since sensitivity is ultimately about the smallest reflectivity that can be detected, a weakly-scattering suspension of microparticles offers a means to access this reflectivity level from a

sample similar to bulk tissue. Such a suspension can be created in one of two ways: with a low concentration of highly scattering particles, or with a high concentration of particles closely index-matched to the surrounding medium. With respect to OCT, the first approach is problematic when the concentration is so low that the image becomes highly heterogeneous, with sparse "hot spots" from individual particles and signal-free regions in between. Achieving different scattering levels requires changing the concentration, which changes only the space between particles. Alternatively, using a high concentration of particles whose refractive index is similar to the surrounding medium generates spatially homogeneous scattering with fully developed speckle, similar to tissue. Changing the index of the medium thus offers a way to alter the scattering level while maintaining homogeneity and speckle. Suspensions like these also provide a consistent signal insensitive to angle/tilt positioning with respect to the OCT beam.

2.4.1 Preparation of microsphere suspensions

A collection of eight scattering suspensions was prepared to provide a range of scattering coefficients close to 0 cm^{-1}. These suspensions comprised silica microspheres with diameter mean 1.57 µm and standard deviation 0.18 µm (Item 25344, Polysciences, Inc., Warrington, PA) in mixtures of deionized water and dimethyl sulfoxide (DMSO, Sigma-Aldrich, St Louis, MO). From the manufacturer's data, the refractive index of the microspheres is approximately 1.43, while that of water is 1.33, and that of DMSO is 1.48. Since the refractive index of a mixture of liquids has a value between their individual refractive indices, the appropriate proportions of DMSO and water yields a refractive index matching that of the silica microspheres, and thus a nearly zero scattering suspension. Slight variations among microspheres and temperature fluctuations prevent perfect index matching to a DMSO-water mixture.

Preparation of the suspensions required several steps. First, the dry silica microspheres were combined with deionized water at a concentration of 10% by weight to create a stock suspension of 3.65×10^{10} particles/mL. The stock concentration was determined by counting particles in a manner described previously [22], using the same microscope setup described in Section 2.3.2. Then, eight mixtures of deionized water and DMSO were prepared, each having a different water-DMSO proportion to yield eight different refractive index values. 57 µL of the stock silica suspension was added to 1 mL of each of the water-DMSO mixtures (final concentration 1.97×10^9 particles/mL), and the resulting suspensions were stored in glass vials with tightly sealing snap caps in the interest of long term stability. A photograph of the eight vials is shown in Fig. 6. Suspension #4 is visibly the most transparent, indicating a near-perfect index match of the microspheres to this water-DMSO mixture.

Fig. 6. Photograph of microsphere suspensions. The scattering level of each suspension can be assessed by visibility of text behind vial.

2.4.2 Characterization of suspensions

Measurements of refractive index and scattering coefficient of the eight suspensions were performed to establish and monitor important optical properties which serve as an absolute reference for sensitivity characterization; results are shown in Table 3. Refractive index at the sodium emission line was measured with a handheld Abbe refractometer (PA202, MISCO

Refractometer, Cleveland, OH), and then the dispersion characteristics of water [20] were applied to estimate refractive index of each suspension (n_{susp}) at 855 nm and 1310 nm. Repeated measurements over an 8 month period revealed n_{susp} uncertainty of ± 0.0003 (one standard deviation).

The scattering coefficient (μ_s) of the eight suspensions was measured via collimated transmittance, applying the Beer-Lambert law to calculate μ_s under the assumption of single scattering (from a statistical standpoint) and no absorption by the microspheres. Collimated transmittance was measured with a custom apparatus consisting of an 830 nm laser diode (LPS-830-FC, Thorlabs, Inc., Newton, NJ) and a detector separated by approximately one meter, with a cuvette in between containing a sample of one of the suspensions or its reference water-DMSO mixture with matching refractive index. Two or three repeated measurements from each suspension were taken over a period of 10 months; Table 3 shows the mean and standard deviation over this time period. The detector for these measurements was either a CCD camera (Alta U2000, Apogee Imaging Systems, Roseville, CA), or a silicon photodiode (818-ST2-UV, Newport Corporation, Irvine, CA) coupled to a power meter (1918-R, Newport Corporation).

To corroborate these measurements, we estimated μ_s values using publicly-available Mie scattering code [23,24] and a Monte Carlo numerical approach to propagate uncertainty in the input parameters for Mie calculations [25]. Two parameters were treated as certain, wavelength (830 nm) and suspension concentration (1.97×10^9 particles/mL), and three parameters were treated as uncertain with Gaussian-distributed values: microsphere diameter (1.57 ± 0.18 μm), medium refractive index n_{medium}, and microsphere refractive index n_{sphere}. Because the microspheres occupy <0.5% of the suspension volume and their refractive index is close to the medium's, we used n_{susp} at 855 nm shown in Table 3 for n_{medium}, after further correcting for dispersion to 830 nm, with the uncertainty stated above (± 0.0003). Our scattering measurements revealed that n_{sphere} was nominally equal to the index of suspension #4 (1.420 at 855 nm, from Table 3), which exhibited nearly zero scattering. n_{sphere} uncertainty was set to ± 0.002 (one standard deviation), since we knew n_{sphere} could not be equal to n_{susp} for suspensions #3 or #5, which exhibited measurable scattering and were ± 0.005 different in index from #4. We then calculated 100,000 μ_s values for each suspension by randomly sampling 100,000 values within each distribution of the three uncertain parameters and combining them with the two certain parameters. The resulting distributions of μ_s are highly non-Gaussian, because μ_s asymptotes to zero in this extremely low scattering regime, but $\log(\mu_s)$ is nearly Gaussian distributed. So in Table 3 we report the mean and standard deviation of each suspension's Mie-estimated $\log(\mu_s)$ distribution. The measured and Mie-estimated $\log(\mu_s)$ means match well within the Mie uncertainties, which are relatively large since μ_s is so close to zero.

Table 3. Refractive index (n_{susp}) and scattering coefficient (μ_s) of the microsphere suspensions

Suspension #	n_{susp}		μ_s (cm^{-1}) @ 830 nm		
	855 nm	1310 nm	Measured	Log of Measured	Log of Mie-estimated
1	1.406	1.401	0.463 ± 0.022	−0.33 ± 0.02	−0.34 ± 0.24
2	1.411	1.406	0.235 ± 0.015	−0.63 ± 0.03	−0.74 ± 0.30
3	1.415	1.410	0.058 ± 0.000	−1.23 ± 0.00	−1.33 ± 0.54
4	1.420	1.415	0.012 ± 0.006	−2.08 ± 0.28	−2.57 ± 0.99
5	1.425	1.420	0.094 ± 0.001	−1.03 ± 0.01	−1.33 ± 0.54
6	1.429	1.424	0.233 ± 0.003	−0.63 ± 0.01	−0.74 ± 0.30
7	1.434	1.429	0.507 ± 0.011	−0.30 ± 0.01	−0.35 ± 0.24
8	1.439	1.434	1.079 ± 0.029	+ 0.03 ± 0.01	−0.08 ± 0.23

To facilitate sensitivity comparisons with the specular surface method, suspension reflectance (R_{susp}) was calculated at the two OCT wavelengths with Eq. (5), based on the

formula provided by Schmitt et al for depth-resolved reflectance [8] for the specific case where depth in the sample is zero. This formula appropriately conveys only the portion of the reflected signal within the coherence length (l_c) and collection aperture of the OCT system:

$$R_{susp} \text{ (dB)} = 10\log\left[2\pi\mu_b(NA)^2 l_c\right]. \tag{5}$$

We calculated backscattering coefficients (μ_b) at 855 and 1310 nm for each suspension with the same Mie scattering code and uncertainty propagation approach described above for μ_s. We set $n_{sphere} = 1.415 \pm 0.002$ at 1310 nm, again from suspension #4. Applying l_c and NA for the two OCT systems from Table 1, we obtained the R_{susp} values shown in Fig. 7. The large uncertainty in μ_b leads to 8-12 dB uncertainty (one standard deviation) in R_{susp}.
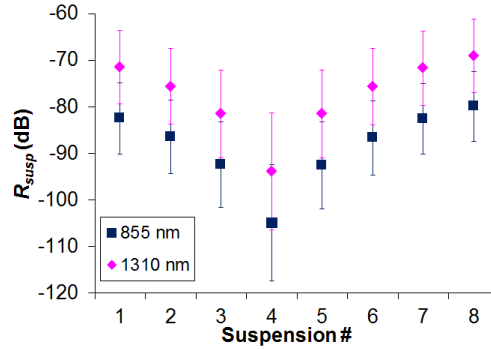

Fig. 7. Reflectance of the microsphere suspensions at zero depth for the two OCT systems. Error bars represent one standard deviation.

3. Results and discussion

3.1 Specular surface

For each of the four system configurations (855 nm, 1310 nm/1.2 mW, 1310 nm/2.3 mW, 1310 nm/4.5 mW), 20 OCT B-scans were captured under two different conditions to obtain the two necessary parameters for SNR calculations: (1) with the reflector removed, to obtain σ_{bg}; (2) with the reflector at the maximum signal position, to obtain I_{samp}.

Figure 8 shows σ_{bg} versus depth, where each σ_{bg} curve is calculated by taking the standard deviation across all the A-scans in a B-scan: 1024 and 500 A-scans respectively for the 855 and 1310 nm systems. The first 19 pixels in depth are excluded because of the presence of autocorrelation signal artifacts. All four exhibit a decrease in magnitude with increasing depth as a result of the signal rolloff effect of SDOCT. Differences in σ_{bg} among the 1310 nm power levels are apparent − higher power yields higher background variability, due to the effect of shot noise.
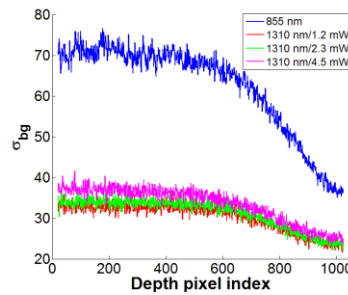

Fig. 8. Standard deviation of background image intensity versus depth.

Pixels 20-400 in depth are a range where σ_{bg} remains relatively constant for all four configurations, so we use this range and all the pixels across the entire width of the B-scan to define a rectangular region of interest (ROI) over which to calculate standard deviation, to determine a single σ_{bg} value for each system configuration. SNR can then be calculated accurately with I_{samp} values extracted from anywhere within this large ROI. OCT image quality and concomitant SNR can be improved by averaging multiple B-scans together to reduce σ_{bg}, but for this study the σ_{bg} value is calculated within a single B-scan to determine fundamental instrument sensitivity with no image quality enhancement. To compute statistics on σ_{bg}, 20 σ_{bg} values were calculated from the 20 separate B-scans acquired with each system configuration; the mean and standard deviation of each set of 20 σ_{bg} values are reported in Table 4.

Figure 9 shows 1.5 mm-wide averaged B-scans with the fused silica reflector positioned to maximize image intensity near the center of the B-scan. We checked B-scans in both lateral scanning axes to verify maximum intensity. These OCT images, and those in subsequent figures in this manuscript, are displayed with linear intensity scaling instead of the conventional logarithmic scaling. The reflector signals are within the ROI defined above for σ_{bg} estimation. The signal intensity tends to drop away from the center of the B-scan since the beam angle is changing from the direction of maximum signal return from the reflector. The 855 nm image is slightly sloped because the beam traverses optical elements within the system which are shifted or tilted off-axis, altering the pathlength asymmetrically.
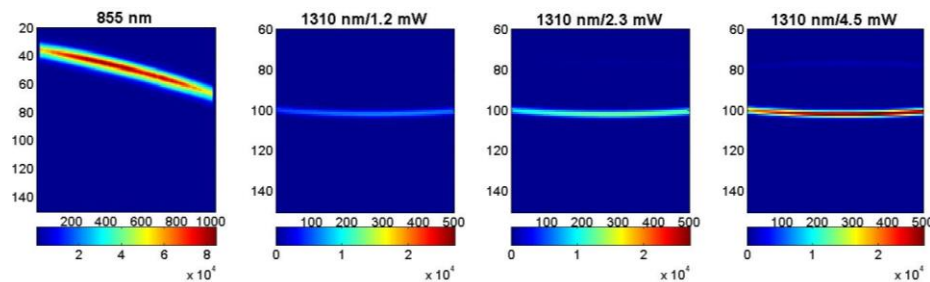

Fig. 9. B-scans of fused silica front surface. Axes are labeled with pixel index. Linear intensity scale colormap is beneath each image.

Since the specular reflection gives rise to a narrow peak in each A-scan, I_{samp} is estimated by averaging the peak intensity values of multiple A-scans at the region of the B-scan with maximum intensity. We first averaged all 20 B-scans together, then averaged the peak values from 10 A-scans for 855 nm and 200 A-scans for 1310 nm to estimate mean I_{samp} values. The lower NA of the 855 nm system means it is more directionally sensitive and thus the intensity remains consistent over a narrower region of the B-scan, so it is reasonable to use fewer A-scans to compute I_{samp}.

Using the R_{samp} and T_{filt} values in Table 2 and the mean I_{samp} and σ_{bg} values in Table 4, SNR_{max} and R_{min} values were calculated with Eqs. (3) and (4) and are also shown in Table 4. The 855 nm system achieves SNR similar to that of the 1310 nm system at 2.3 mW, with less than 1/3 the power but with nearly 4 times longer integration time to compensate. The larger spot of the 855 nm system means its irradiance is ~6 times less than 1310 nm irradiance at 2.3 mW, and its NA is 3 times less. However, by placing a specular surface normal to the beam and at its focus, this SNR measurement technique ideally couples all the reflected light back into the system, so spot size and NA are not expected to influence the SNR measurement.

Table 4. SNR values for the specular surface method

OCT configuration	I_{samp} (counts)	σ_{bg} (counts)	SNR_{max} (dB)	R_{min}
855 nm	83300 ± 1150	70.0 ± 0.25	94.6	3.46E-10
1310 nm/1.2 mW	6370 ± 5	31.9 ± 0.04	87.8	1.68E-9
1310 nm/2.3 mW	12900 ± 10	33.9 ± 0.03	93.4	4.61E-10
1310 nm/4.5 mW	26700 ± 20	37.3 ± 0.06	98.8	1.30E-10

3.2 Laser-inscribed phantom

When OCT imaging the sensitivity region of the phantom, it was tilted slightly with respect to the beam to discard the specular reflection from the surface. Each group of lines is 1.5 mm wide, equal to the B-scan width, so each group was imaged separately. B-scans were oriented perpendicular to the lines, resulting in bright spots in the images corresponding to the cross-sections of the lines. The focus was placed midway axially between the shallowest and deepest line. 40 B-scans were captured with each acquisition, offset from one another by 5 μm along the lines. Figure 10 shows B-scans of Groups 1 and 6, the lowest and highest reflectivity groups, for all four system configurations.
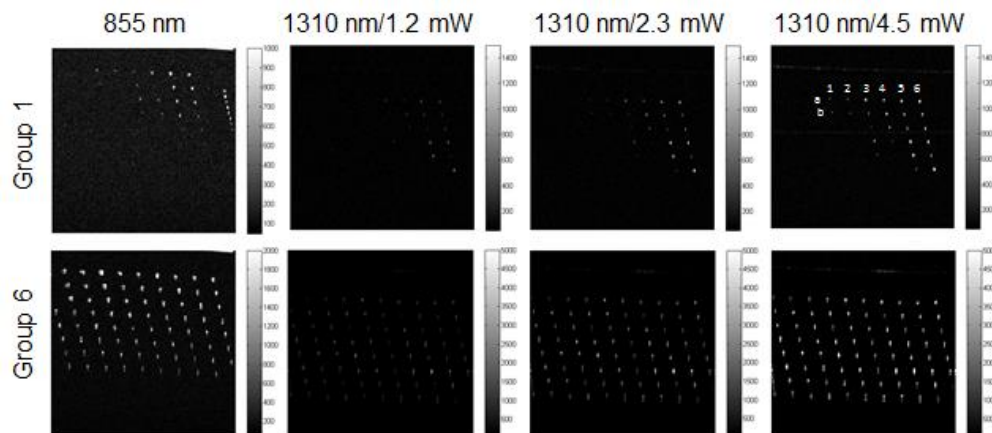

Fig. 10. B-scans of Groups 1 and 6 in sensitivity region of laser-inscribed phantom. Images are 1.5 mm wide × 1.5 mm optical depth. Linear intensity scale is to the right of each image.

Only Group 1 was considered for SNR analysis, since only this group produced OCT intensities close to the sensitivity-defined threshold SNR value of 0 dB. All the other groups yielded SNR values well above 1. We identified the 12 lines in the top two rows to sufficiently represent the SNR range of this group, labeled in the upper right image of Fig. 10. At each line's signal location in a B-scan, I_{samp} was calculated from the mean of an 8 × 8 pixel (lateral × axial) ROI for the 855 nm system and of a 5 × 3 pixel ROI for the 1310 nm system, with the ROI centered at the line's brightest point. These ROI sizes correspond to the lateral and axial FWHM of the spots in each system's images and ensure a fair comparison between the two OCT systems. Their FWHM values differ laterally because of differences in spot size and axially because of differences in source wavelength, coherence length, and spectrometer design.

To estimate I_{samp} for each system configuration, the ROI means were calculated after averaging all 40 B-scans together. Using these mean I_{samp} values along with the values of σ_{bg} from Table 4, SNR was calculated per Eq. (1b). Figure 11 shows a graph of SNR from each of the 12 lines, identified as shown in the 1310 nm/4.5 mW image of Fig. 10. The SNR values for the 855 nm system now closely match the 1310 nm values at 1.2 mW, instead of matching at 2.3 mW with the system SNR. This shift in the relative performance between the two systems arises because spot size and NA are now having an effect, given the nature of the

reflective structures. The lines act nearly as point reflectors along the B-scan lateral axis, so the reflected signal level becomes more dependent on irradiance, as compared to a continuous specular surface, where only the power level matters and not spot size. In addition, the small size and heterogeneous nature of the lines means light is backscattered over a range of angles around 180° instead of just being specularly reflected, so more light is likely to fall outside the smaller collection aperture of the 855 nm system. It is important to note that the SNR values depend on the axial position of the beam focus; our choice of focus position beneath the analyzed lines reduced the SNR below what could be observed with this phantom.
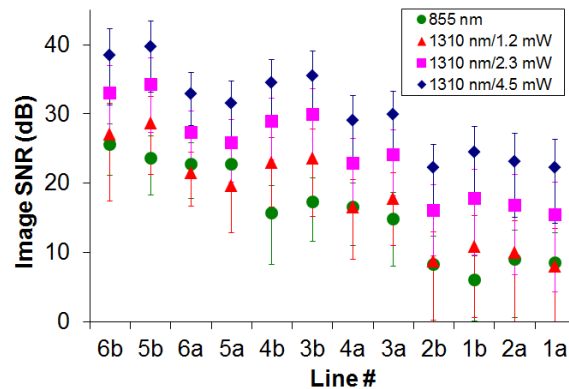

Fig. 11. Image SNR values measured for 12 Group 1 lines shown in Fig. 10.

An alternate use of the sensitivity region of the laser-inscribed phantom is for a visual test, e.g., to identify how many lines can or cannot be visualized, since observation of scattering from individual microscale structures is an important task with OCT. In Fig. 10, individual lines in Group 1 are difficult to visualize, which results from their weak reflectance plus several additional factors: intensity scaling of the image, small size of the spots, variability of the spot brightness across the line. But as Fig. 11 indicates, the mean SNR of even the least reflective lines in the top two rows of Group 1 is well above the detectability threshold of 0 dB, although the variability of the lines' reflectivity causes the SNR error bars for the four least reflective lines to approach/cross 0 dB for the 1310 nm/1.2 mW and 855 nm configurations. Therefore, the information gathered from a visual test is quite different than what the quantitative SNR calculations reveal.

A proper visualization test requires specific image acquisition parameters and image display conditions. For example, real-time averaging of multiple B-scans across a C-scan to better visualize the lines is possible only if the bright spots appear in the same locations in each B-scan, which requires precise alignment of the phantom with respect to the OCT beam. The logarithmic scaling typically applied to OCT intensities for viewing would also have a tremendous impact. Optimizing all these factors is beyond the scope of this study. Whether for qualitative or quantitative sensitivity analysis, this phantom would benefit from having less reflective structures (e.g., through a different laser inscription method) to more closely approach the 0 dB SNR threshold. This feature is even more important considering that more sensitive OCT systems are certain to exist or be developed.

3.3 Microsphere suspension phantoms

The eight suspensions were imaged with the four OCT configurations, taking 20 repeated B-scans of each suspension. The beam focus was axially positioned just beneath the vial-suspension interface. The B-scan direction was along the length of the vial off the vial's centerline to direct specular reflections away from the OCT front optic and thus reduce the brightness of the vial-suspension interface signal. Prior to imaging, each vial was shaken by

hand to ensure a homogeneous distribution of particles throughout the vial. Unlike the OCT imaging done with the laser-inscribed phantom, it was not necessary to offset the B-scans from one another when imaging the suspensions because each B-scan samples a different part of the suspension through random motion of the particles. Figure 12 shows images of the suspensions after averaging the 20 B-scans. The interface between the vial glass and the suspension can be seen as a slanted line with irregular hot spots near the top of each image, with the signal-free glass region above and suspension below. Hot spots within the suspension region are also noticeable, due to local imperfections in microsphere geometry or refractive index.
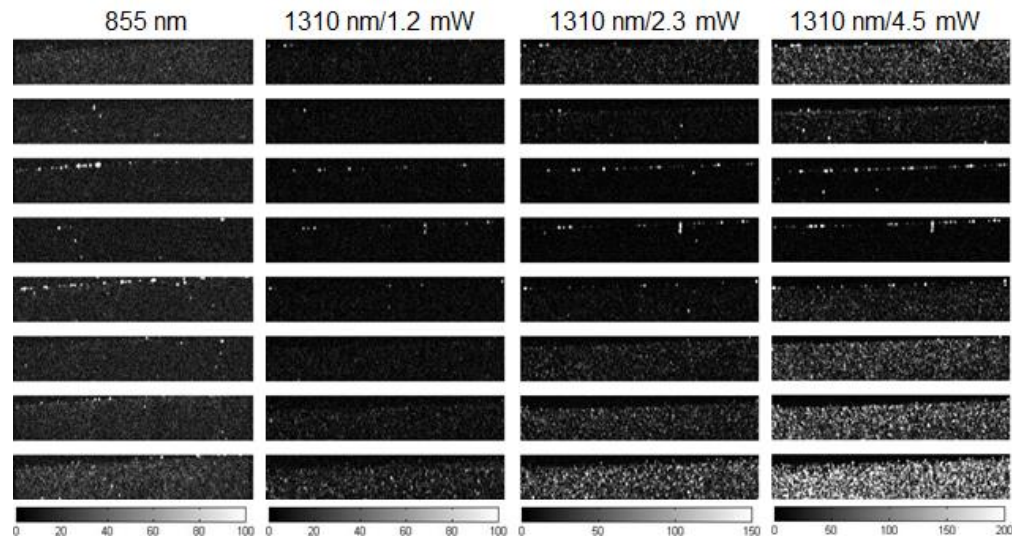

Fig. 12. Average B-scans of the eight suspensions. Images are ordered from suspension #1 at top to #8 at bottom, and are 1500 μm wide × 280 μm optical depth. Linear intensity scale at the bottom of each column applies to all the images in that column.

To estimate I_{samp} from the suspensions, the mean of a ROI 400 μm wide and 100 μm in optical depth was taken just beneath the vial-suspension interface after averaging all 20 B-scans together. We chose a combination of ROI size and B-scan count for averaging which prevents speckle variability from affecting the I_{samp} estimate. SNR was calculated again using the values of σ_{bg} from Table 4, and the SNR values are graphed in Fig. 13. Unlike the laser-inscribed phantom whose features are generally too reflective to clearly cross below the detectability threshold, the majority of scattering levels available in these suspensions was well below the detectability threshold. Still, the large signal-generating area and averaging of multiple B-scans enable visualization of signal even at these exceptionally low SNR levels.
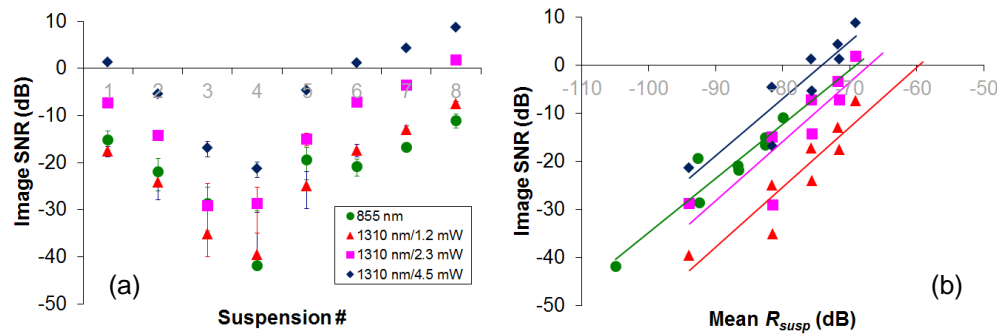
Fig. 13. Image SNR measured from the eight microsphere suspensions, plotted against (a) suspension number and (b) mean R_{susp}. Error bars are excluded from (b) for visual clarity.

The linear fits shown in Fig. 13(b) have strong correlation coefficients, between 0.77 and 0.90. Using these fits we estimated R_{min} by the value of R_{susp} where each line crosses 0 dB SNR, then determined SNR_{max} as the inverse of R_{min} [Eq. (3)]. Table 5 shows these suspension-based SNR_{max} values are 25-28 dB lower than those measured with the conventional specular surface method, though the relative sensitivity among the OCT configurations is strikingly consistent between the two methods. Furthermore, the slopes of all the lines in Fig. 13(b) are greater than unity (1.1-1.2), which on a log-log plot indicates a nonlinear relationship between the variables. Therefore, our results suggest the expected linear relationship between SNR and sample reflectance [Eq. (2a)] does not hold, at least in this exceptionally low signal regime. Additional work is necessary to better understand the nature and origins of this nonlinear behavior, especially in light of the large uncertainty in R_{susp}. In any case, the 8-12 dB uncertainty is not large enough to explain the much larger difference in SNR_{max} between the suspensions and the specular surface. The suspension-based R_{min}/SNR_{max} values are likely more relevant estimates than the specular surface estimates since they originate from measurements of samples with tissue-like turbidity yielding SNR close to zero, and R_{susp} incorporates effects of the system illumination/collection parameters which strongly influence OCT sensitivity. The validity of this new sensitivity measurement method is supported by its consistency with the conventional method when comparing the relative sensitivity of two different OCT configurations, even though the absolute values are very different.

Table 5. SNR_{max} estimated with microsphere suspensions and specular surface

OCT configuration	SNR_{max} (dB)	
	Microsphere suspensions	Specular surface
1310 nm/4.5 mW	74.1	98.8
855 nm	69.0	94.6
1310 nm/2.3 mW	67.1	93.4
1310 nm/1.2 mW	59.6	87.8

4. Conclusions

Table 6 summarizes the advantages and disadvantages of the three sensitivity assessment methods presented in this study. The two new phantom-based methods require some modification to extend their range of OCT sensitivity challenge: the laser-inscribed phantom needs more structures with lower reflectivity, and more highly scattering suspensions would be useful. But for an OCT user both methods offer important advantages to the specular surface method, mainly because they offer a means to spot-check sensitivity through simple visualization of the signal level in an OCT image. Subtle changes in overall system performance can be detected quickly. The main disadvantage of the suspensions is their liquid

format which could yield inconsistent signals if ambient temperature fluctuates significantly or if the particles are not homogeneously redistributed before each measurement, though we observed reasonable consistency over a 10 month period. The laser-inscribed phantom's main weakness is the lack of traceability to a standardized unit, so either a reliable means of quantifying the lines' reflectivity or widespread acceptance across the OCT community is necessary to standardize this phantom.

In conclusion, we have detailed an established approach of assessing OCT sensitivity and examined two types of phantoms that can fill an important role in sensitivity assessment. The phantoms provide a fuller understanding of true OCT system detection limits, in a manner convenient for the OCT engineer and user. We have revealed a potential OCT system nonlinearity in the low signal regime which warrants further investigation.

Table 6. Key characteristics* of the sensitivity assessment methods in this study

	Specular surface	Laser-inscribed phantom	Microsphere suspension phantoms
Acceptance by OCT community	Well-established	Recently commercially-available	Not yet known
Ease of measurement	Precise reflector positioning required	Simple placement; insensitive to angle	Simple placement; insensitive to angle
Ease of data analysis	Data transfer and calculations required	Visualization possible	Visualization possible
Standardized result?	Yes, reflector is calibrated	No, reflectivity of lines is unknown and variable	Yes, suspension optical properties are known
Stability of materials	Highly stable	Highly stable	Liquid refractive index is more sensitive to ambient temperature than solids; inhomogeneous particle distribution possible
Relevance to OCT performance in tissue	Likely overestimates sensitivity	Signal levels may be comparable to tissue	Low backscattering turbid media is very tissue-like

*Advantages in green, disadvantages in red

Acknowledgments